Numerical Study of Simulated Uniform Corrosion Tests

Tsai-Fu Chuang*

Assistant Professor of Department of Landscape Architecture, MingDao University

ABSTRACT

In this paper, a smeared crack model is used to model the behaviour of simulated corrosion tests. This model has been implemented into a FE program (LUSAS) [1] to investigate the expansion of the simulated bars and the failure pressures. This program (LUSAS) contains a material model interface (MMI) that allows users to develop computer code for material models then link the codes to the main program in such a way that the user code controls the material behaviour of the specified elements. A series of simulated corrosion experiments performed by Williamson and Clark [2] have been chosen for comparison. For the finite element calculation, a two-dimensional plane strain model and QPN8 (LUSAS) elements was chosen. The numerical calculations show that the failure pressures obtained from the numerical analysis agree well with the experimental ones. Also, the numerical calculations show that the assumption of uniform bar expansion is reasonable.

Keywords: corrosion, cracking model, finite element method

混凝土鏽蝕試驗的數值模擬

莊財福*

明道大學造園景觀系助理教授

摘要

本文採用一個混凝土裂縫模型(cracking model)用來模擬混凝土鏽蝕試驗的行為。此一數值模型以程式語言完成並經編譯無問題後,再連結於有限元素法軟體 LUSAS 之主程式上。LUSAS 主程式中包含一個材料模式介面(MMI)允許使用者自行發展電腦材料副程式,並可將此材料副程式與 LUSAS 主程式連結。以此種方式,使用者自行發展的材料副程式,則可應用於使用者指定的材料元素上。而實驗數據則採用 Williamson 和 Clark 所進行的鏽蝕試驗。本研究的數值分析中,採用了二維的平面應變 (Two-dimensional plane strain models),而荷重則採用位移控制(displacement control)來進行。研究結果顯示數值破裂壓力與實驗結果相當吻合。而數值分析結果亦顯示混凝土均勻膨脹為合理之假設。

關鍵字:鏽蝕,裂縫模型,有限元素法

I. INTRODUCTION

A very early finite element codes to model the crack behaviour of concrete was that proposed by Bazant and Cedolin [3]. They also proposed a fracture energy criterion to analyse a rectangular reinforced concrete panel for crack propagation. Furthermore, they also explained the reason for the "mesh dependence". The explanation given for this spurious mesh sensitivity, or inobjectivity, was that the value of the stress in an element ahead of a crack front depends on the width of the crack band. Also, the width depends on the element size because the crack width is the effective width of the area or volume associated with a particular element sampling point. Thus, the smaller the elements, the sharper the cracks and the higher the stress in the element ahead of the crack tip.

The methods proposed by Bazant and Cedolin [3] drew attention to the fracture energy and suggested that the answer to the spurious mesh sensitivity was to apply fracture mechanics.

Doubtless, these were problems that could be overcome, and, a fracture energy dependent softening model was then proposed by Bazant and Oh [4] for application to the smeared crack model. They suggested that cracks occurred in a band or zone rather than a line, and also, that over the zone, a fracture strain could be defined which was equal to the sum of the openings of the individual micro-cracks divided by the width of the fracture process zone. Thus, their crack criterion for governing the crack initiation was again assumed to be the tensile strength and once a crack had started, the stress was then followed by a decreasing linear function of the increasing fracture strain. The fracture energy, per unit area of crack, could then be equated to the area under the stress/fracture strain curve multiplied by the width of the fracture process zone. In the smeared crack approach, a crack is assumed to be spread over the width associated with a sampling position and thus the 'numerical' crack process zone was assumed to depend upon the size of the element. Bazant and Oh [4] simply equated the 'characteristic length' of an element with the width of the crack process zone.

This model was rapidly adopted by other investigators[5-7] and become a well-established way of modelling concrete fracture and this approach is also adopted in this paper.

Reinforced concrete is a widely used, economical, versatile and generally durable construction material. Premature deterioration of reinforced concrete is, however, a subject which is currently of great concern with the major cause being corrosion of reinforcing steel which is caused by either carbonation or ingress of chlorides.

Prior to the onset of corrosion of reinforcing steel some aggressive species must be transported through the concrete cover, termed 'covercrete', to the reinforcement [2]. The life of a structure in terms of time to replacement or repair may be defined as the time taken for this transport to occur and corrosion to commence. This is known as the initiation period after a model developed by Tuutti [8]. Alternatively life may be defined as the point when corrosion reaches some pre-determined unacceptable level which is generally the appearance of surface cracking. The time taken to reach this point from the onset of corrosion is known as the propagation period, again after Tuutti [8]. The length of the initiation period depends upon the thickness, permeability and porosity of the covercrete. Once corrosion has begun the time taken to crack the cover depends both upon the rate at which corrosion continues and the resistance to cracking of the cover. Corrosion behaviour of reinforced concrete is, therefore,a function of both the transport properties and cracking resistance of concrete in the cover zone [2].

In this paper, a fixed smeared crack model is used to model a series of simulated uniform corrosion experiments performed by Williamson and Clark[2]. The main purpose of this calculation is to provide further information to improve the understanding of this experiment. Main attentions have been paid to the relationship between the failure pressure and the c/d ratios (Cover(c)/Diameter(d)) and whether the assumption of uniform bar expansion is reasonable.

II. METHOD OF NUMERICAL ANALYSIS

The basic fracture model used is the "smeared fixed crack model" which has a maximum tensile stress criterion for initial crack formation and subsequently the concrete is treated as orthotropic with the material strain softening in the direction normal to the crack. A second crack is permitted to form, orthogonal to the first, if the tensile stress in that direction exceeds the limiting value. The concept of fixed crack model is that this model has a memory of the angle of initial crack. No matter whether a subsequent principal stress has exceeded the ultimate fracture stress, this memory will not be erased. In this study, a flat stepped softening curve(Figure 1) is proposed which is inspired from that suggested by Nilsson and Oldenburg [9] (Figure 1). The advantage of using the flat stepped softening curve is that it can improve the stability of the strain softening problem [6]. One reason for the numerical instability of the strain softening problem is that when negative moduli are used, the structure stiffness matrix can become non-positive-definite. This implies that a unique solution is not guaranteed.
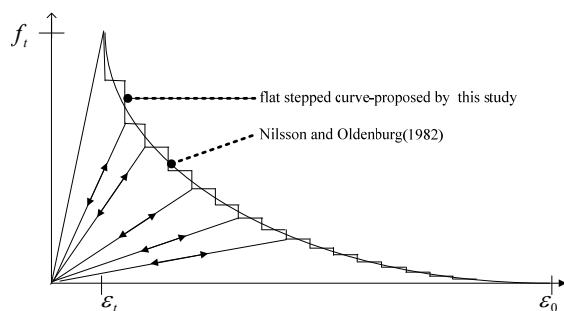
Fig. 1. Flat stepped softening curve for tension.

The shear modulus G, in the cracked D-matrix, is multiplied by a shear retention factor β (Figure 2) which is a function of the normal crack strain..

The cracked compliance matrix for a single crack is

$$
\begin{bmatrix} \Delta \varepsilon_{11} \\ \Delta \varepsilon_{22} \\ \Delta \gamma_{12} \end{bmatrix} = \begin{bmatrix} 1/D_1 & 0 & 0 \\ 0 & 1/D_2 & 0 \\ 0 & 0 & 1/\beta G \end{bmatrix} \begin{bmatrix} \Delta \sigma_{11} \\ \Delta \sigma_{22} \\ \Delta \tau_{12} \end{bmatrix}
$$

(1)

Hence the D matrix can be represented as

$$
Dcr = \begin{bmatrix} D_1(\varepsilon_{11}) & 0 & 0 \\ 0 & D_2(\varepsilon_{22}) & 0 \\ 0 & 0 & \beta G \end{bmatrix}
$$

(2)

where $D_1(\varepsilon_{11})$ and $D_2(\varepsilon_{22})$ are derived from the slope of the softening curve.

$D_1(\varepsilon_{11})$ = Tangential stiffness modulus in direction 1 i.e. normal to the crack plane.

$D_2(\varepsilon_{22})$ = Tangential stiffness modulus in direction 2 i.e. perpendicular to direction 1.

β = Shear retention factor which is a function of the normal crack strain (ε1 or ε2).

G = Elastic shear modulus.

ε11 = Total fracture strain in direction 1 i.e. normal to the crack plane.

ε22 = Total fracture strain in direction 2 i.e. perpendicular to 1 direction.

$\Delta \varepsilon_{11}$ = Concrete strain increment in direction 1 i.e. normal to the crack plane.

$\Delta \varepsilon_{22}$ = Concrete strain increment in direction 2 i.e. perpendicular to direction 1.

$\Delta \gamma_{12}$ = Shear strain increment.

$\Delta \sigma_{11}, \Delta \sigma_{22}$ = Principal stress increments.

$\Delta \tau_{12}$ = Shear stress increment.

The mode I fracture energy can be derived by multiplying the area under the σ-ε curve with the characteristic length le. Therefore, the mode I fracture energy Gf can be represented as follows:

$$
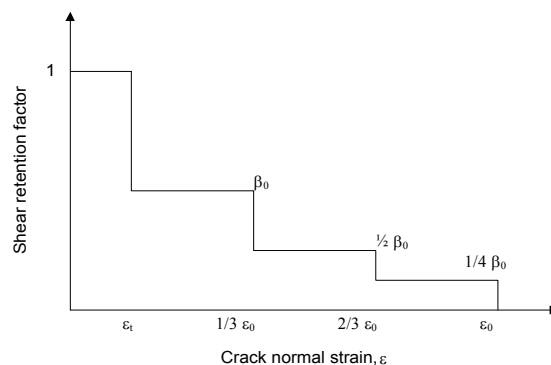G_f = l_e \int_0^{\varepsilon_0} \sigma d\varepsilon = l_e \times \text{area under the curve} \quad (3)
$$

Fig. 2. shear retention facto.

where le = characteristic length and is taken as the cubic root of the volume associated with an element sampling point. Gf = Fracture energy per unit volume; ε0 = ultimate fracture strain.

In the current study, the equations of the softening curve (Figure 1) suggested by Nilsson and Oldenburg [9] is shown as bellows:

$$\sigma = f_t \times \exp(\frac{\varepsilon_t - \varepsilon}{\alpha}) \tag{4}$$

$$\alpha = (G_F - 0.5 \times f_t \times \varepsilon_t \times 1_e)/(f_t \times 1_e) \tag{5}$$

where f_t = uniaxial tensile strength, εt = elastic ultimate strain. The compressive behaviour of this model uses non-linear hardening plasticity theory with a yield criterion that is obtained by fitting biaxial experimental results.

2.1 Yield Criterion

In this paper, a yield criterion proposed by Owen et al. [10] was employed. This criterion is formulated in terms of the first two stress invariants and only two material parameters are involved in its definition.

$$F(I_1, J_2) = \left[\beta(3J_2) + \alpha I_1\right]^{1/2} = \overline{\sigma} \tag{6}$$

where α and β are material parameters and $\overline{\sigma}$ is the effective stress (or equivalent yield stress) taken as the compressive stress from an uniaxial test. $I_1 = \sigma_1 + \sigma_2 + \sigma_3$,and $J_2 = \frac{1}{6}\left[(\sigma_1 - \sigma_2)^2 + (\sigma_2 - \sigma_3)^2 + (\sigma_3 - \sigma_1)^2\right]$ .In terms of principal stresses, the expression for yielding can be written as,

$$\beta\left[\frac{1}{2}\left[(\sigma_1 - \sigma_2)^2 + (\sigma_2 - \sigma_3)^2 + (\sigma_3 - \sigma_1)^2\right]\right] + \alpha(\sigma_1 + \sigma_2 + \sigma_3) = \overline{\sigma}^2 \tag{7}$$

where σ_1, σ_2, and σ_3 are the principal stresses referring to the principal stress axes, 1, 2, and 3.

To fit the data of Kuper et. al [11], the parameters take the values:

$$\alpha = 0.355 \,\overline{\sigma}, \quad \beta = 1.355$$

Substituting the above two values into (7) and rearranging gives

$$\overline{\sigma} = CI_1 + \sqrt{C^2 I_1^2 + DJ_2} = 0 \tag{8}$$

where C = 0.1775, D = 4.065; $\overline{\sigma}$ =

equivalent yield stress.

2.2 Flow Rule

The flow rule is assumed to be associated to the compressive yield surface. The gradient of the yield surface is given by :

$$\frac{\partial F}{\partial \sigma_{ij}} = \frac{\partial F}{\partial I_1}\frac{\partial I_1}{\partial \sigma_{ij}} + \frac{\partial F}{\partial J_2}\frac{\partial J_2}{\partial \sigma_{ij}} \tag{9}$$

where

$$\frac{\partial F}{\partial I_1} = C + \frac{C^2 I_1}{\sqrt{C^2 I_1^2 + DJ_2}} \tag{10}$$

$$\frac{\partial F}{\partial J_2} = C + \frac{D}{2\sqrt{C^2 I_1^2 + DJ_2}} \tag{11}$$

$$\frac{\partial I_1}{\partial \sigma_{ij}} = \delta_{ij} \tag{12}$$

2. 3 Hardening Rule

The hardening rule adopted in concrete is usually obtained by fitting the experimental data. In this study, the hardening rule proposed by Jefferson and Wright [6]. The hardening parameter is obtained from Saenz's equation [12].

Saenz's equation can be expressed as：

$$\overline{\sigma} = \frac{E_0 \varepsilon_u}{1 + \left[\frac{E_0}{E_s} - 2\right]\frac{\varepsilon_u}{\varepsilon_c'} + \left(\frac{\varepsilon_u}{\varepsilon_c'}\right)^2} \tag{13}$$

where E_o = initial Young's modulus, ε_u = uniaxial strain, ε_c' = uniaxial strain at peak stress, σ_c = peak uniaxial stress.

$$E_s = \frac{\sigma_c'}{\varepsilon_c'}$$

From the definition of H (Hardening parameter), the following equation can be obtained:

$$H = \frac{d\sigma}{d\varepsilon_p} = \frac{d\sigma}{d\varepsilon - d\varepsilon_e} = \frac{1}{\frac{d\varepsilon}{d\sigma} - \frac{d\varepsilon_e}{d\sigma}} = \frac{\frac{d\sigma}{d\varepsilon}}{1 - \frac{d\sigma}{d\varepsilon}\frac{d\varepsilon_e}{d\sigma}} = \frac{E_T}{1 - E_T / E_o} \tag{14}$$

where σ = stress, ε = strain, ε_p = plastic strain, ε_e = elastic strain.

$$E_T = \frac{d\sigma}{d\varepsilon}$$

III. EXPERIMENT SETUP

A series of experiments have been performed by Williamson and Clark [2] to investigate the effect of the cover concrete quality on the corrosion behaviour of reinforced concrete. In their tests hydraulic pressurisation of a hollow concrete specimen was used to simulate the expansive pressure created by uniform corrosion. Uniform corrosion pressure was modelled by using a hydraulic jack to pressurise a soft P.V.C tube inserted into the hollow concrete specimen.

The specimens used by Williamson and Clark were 150 mm concrete cubes with 2 holes of 8 mm, or 16 mm in diameter on its side (testing one hole at a time), and the cover thickness were 4 mm, 8 mm and 16 mm. The concrete properties for the simulated corrosion test are shown in Table 1. The Material properties of the P.V.C tube are shown in Table 2, and the designation of the test is shown in Table 3. Table 4 shows the range of the ultimate strengths of the experimental results and the experimental crack pattern is given in Figure 3

Fig. 3. Experimental arrangement and crack pattern of simulated.

Table. 1 Concrete properties for the simulated corrosion test

Young's modulus	E = 28580N/mm2
Poisson's ratio	ν = 0.2
Uniaxial compressive strength	fc = 21.6 N/mm2
Uniaxial tensile strength	ft = 2.16 N/mm2
Uniaxial strain at peak compressive strength	εc' = 0.0022
Fracture energy	Gf = 0.1 N/mm
Initial shear retention factor	β = 0.1

Table. 2 Material properties of the P.V.C tube

Young's modulus	E = 2858 N/mm2
Poisson's ratio	ν = 0.2

Table. 3 Designation of simulated corrosion test

Test Designation	Ratio	Cover (c)	Diameter (d)
C4D8S2	c/d=0.5	4 mm	8 mm
C8D8S2	c/d=1	8 mm	8 mm
C16D8S2	c/d=2	16 mm	8 mm

Table. 4 Experimental results of C4D8S2, C8D8S2 and C16D8S2

Experimental Designation	Number of specimen	Range of the ultimate strength applied by the hydraulic jack
1. C4D8S2	6	4 ~ 5 N/mm2
2. C8D8S2	6	7 ~ 8 N/mm2
3. C16D8S2	6	12 ~ 15 N/mm2

IV. NUMERICAL ANALYSIS

The corrosion test is analysed with the proposed fixed crack model. A two-dimensional plane strain model is chosen for simulating the concrete cubes. The reasons are shown as follows:

For typical plane strain problems the thickness dimension normal to a certain plane (say the xy plane) is large compared with the

typical dimensions in the xy plane and the body is subject to loads in the xy plane only, Also, It may be assumed that the displacements in the z direction are negligible. For typical plane stress problems, the dimension in the out-of-plane should be very small relative with the plane dimensions in the xy plane. Stresses are assumed to be constant through the thickness of the out-of-plane.

It can be seen that none of the above two selections are perfectly suitable with the concrete cubes. However, it is known that the concrete cubes are subject to loads in the in-plane direction only, therefore,the displacement in the out-of-plane direction is quite small and its magnitude is influenced by the Poisson's ratio only. For this reason, a two-dimensional plane strain model is chosen for this study.

The soft P.V.C. tube is modelled as an elastic material (see Table 2), and the arc-length method available in LUSAS is chosen for the simulation of softening behaviour.

V. ANALYSIS RESULT

5.1 Mesh dependency study

For each cover thickness, i.e. 4 mm, 8 mm and 16 mm, two finite element meshes are employed to show the influence of mesh refinement on the pressure-displacement curves as shown in Figures 4 to 9. The position selected for plotting the pressure-displacement curve is the outside point of the concrete cover which lies on the middle of the edge line as shown in Figure 10.

The pressure-displacement curves of the corrosion specimen obtained with the two meshes for each cover thickness are shown in Figures 11 to 13. It can be observed that the reasons the coarse and refined finite element meshes are in very good agreement. Based on this observation, all the subsequent studies are performed using only the coarse mesh.
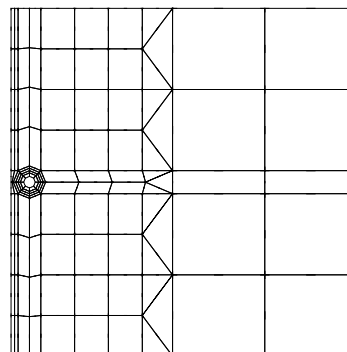
Fig. 4. Mesh I of case C4D8S2 with c/d=0.5.
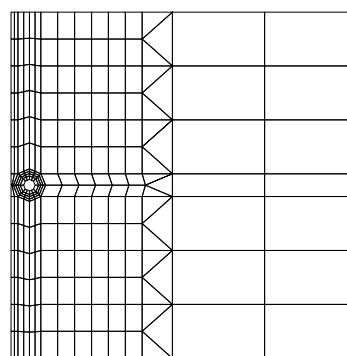
Fig. 5. Mesh II of case C4D8S2 with c/d=0.5.
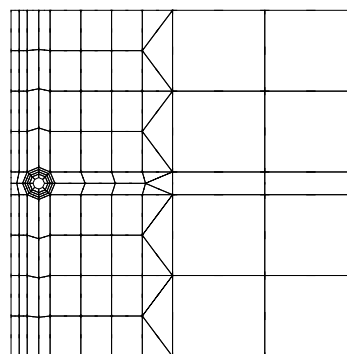
Fig. 6. Mesh I of case C8D8S2 with c/d=1.0.
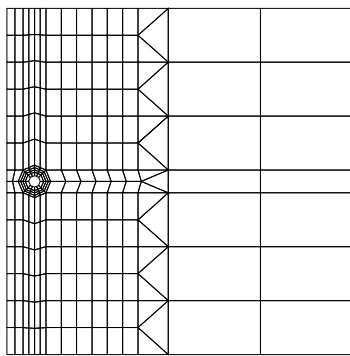
Fig. 7. Mesh II of case C8D8S2 with c/d=1.0.
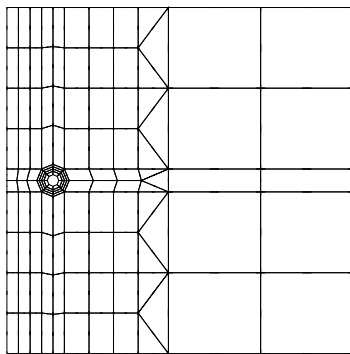
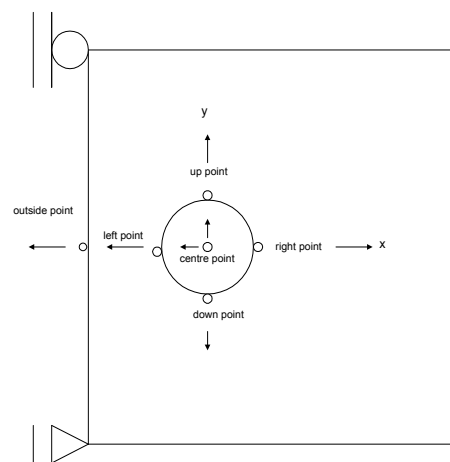Fig. 8. Mesh I of case C16D8S2 with c/d=2.0.

Fig. 9. Mesh II of case C16D8S2 with c/d=2.0.

Fig. 10. The position, designation and direction of the selected points.

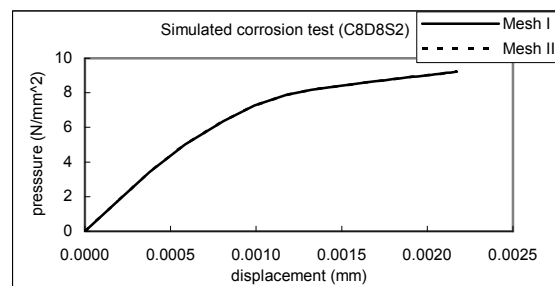Fig. 11. Mesh dependency test with ratio c/d=0.5.

Fig. 12. Mesh dependency test with ratio c/d=1.0.

5.2 Displacement - pressure curves

Figure 10 indicates that the selected points are marked as the Outside-point, Left-point, Up-point, Right-point and Down-point. In addition, the 4 points that are located on the edge of the simulated bar, i.e. Left-point, Up-point, Right-point and Down-point, are called Inside-points. The displacement-pressure curves for C4D8S2 (c/d=0.5) obtained from the numerical analysis are shown in Figures 14 ~ 15.

Figure 14 shows that all the selected points exhibit a positive correlation with the expansive pressure. When the result obtained from the Up-point is compared with that from the Down-point, it can be observed that the results

of the Up-point exhibit higher value than the Down-point. However, due to the symmetry of the specimen, the two points should exhibit the same results. The reason for the difference is that the deformation of the simulated bar, the whole specimen will move toward the roller side (refer to Figure 10).

In order to obtain the net deformation at the Up-point and Down-point, the absolute displacement of the Up-point and Down-point is reduced by the displacement of the centre of the simulated bar and it is called net displacement.

Figure 15 shows the net displacement-pressure curves of the selected points. Comparing the net displacement obtained from the 4 Inside-points, it can be seen that the Left-point has larger value than the Up-point and Down-point. Additionally, the Up-point and Down-point displace more than the Right-point. The reason for this can be considered from the view of resistant stiffness and thickness for the 4 Inside-points. For the Left-point, the thickness of the cover is 4 mm. For the Up-point and Down-point, the thickness of the cover can be regarded as half of the length (i.e. $\frac{1}{2} \times 150\,\text{mm}$) of this specimen minus half the bar size. Additionally, the thickness of the cover for Right-point can be regarded as the total length of this specimen minus the bar size and concrete cover. Therefore, from the view of stiffness, since the Right-point has the bigger cover thickness, the net displacement at this point will have the smallest value.

Figure 16 shows the reduction of the concrete cover and the expansion of the simulated bar in the x and y directions. It can be

seen that the pressure increases with the reduction of cover. When the elongation of the simulated bar in the x direction is compared with the y direction, it can be seen that the result in the x direction exhibits a close result to that in the y direction.

The displacement-pressure curves for C8D8S2 (c/d=1.0) obtained from the numerical analysis are next shown. The absolute displacement-pressure curves of the selected points are shown in Figure 17. Figure 18 shows the net displacement-pressure curves of the selected points. Figure 19 shows the reduction of the concrete cover and the expansion of the simulated bar in the x and y directions.

The displacement-pressure curves for C16D8S2 (c/d=2.0) obtained from the numerical analysis are next shown. The absolute displacement-pressure curves of the selected points are shown in Figure 20. Figure 21 shows the net displacement-pressure curves of the selected points. Figure 22 shows the reduction of the concrete cover and the expansion of the simulated bar for x and y direction. Again, these results show similar behaviour as test C4D8S2 (c/d=0.5).

The comparison of the elongation of the simulated bar in x direction between various cover concrete ratio, i.e. c/d=0.5, 1.0 and 2.0, is shown in Figure 23 and the comparison in y direction is shown in Figure 24. It can be observed that the elongations of the simulated bar in both directions reduce with increasing concrete ratio. Additionally, it can be seen that elongations for c/d= 1.0 and 2.0 are very similar.
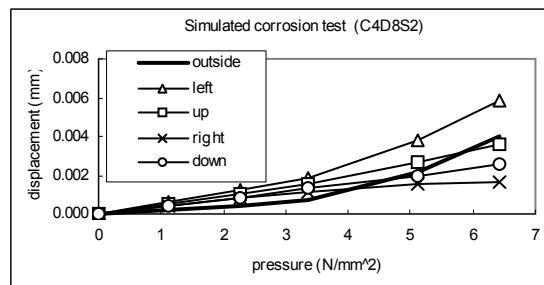

Fig. 13. Mesh dependency test with ratio c/d=2.

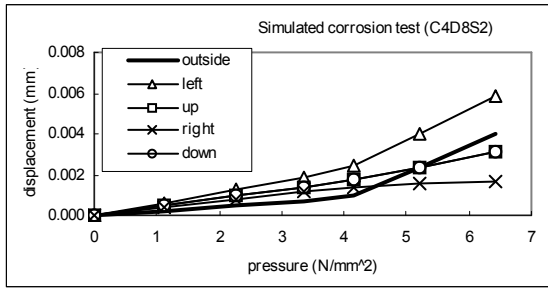Fig. 14. Displacement-pressure curves from numerical result (c/d=0.5).

Fig. 15. Net displacement-pressure curves from numerical result (c/d=0.5).
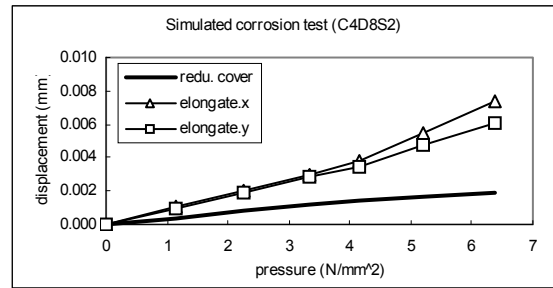

Fig. 16. The reduction of the cover and elongation of the simulated bar.
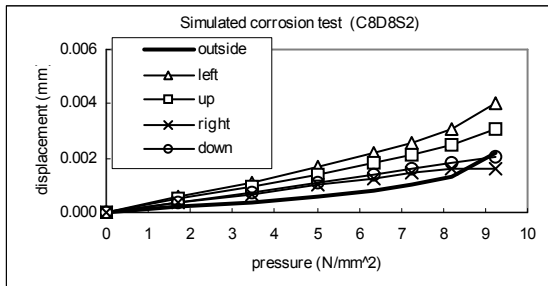

Fig..17. Displacement-pressure curves of numerical result (C8D8S2).
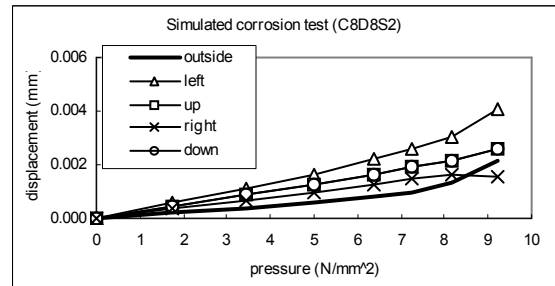

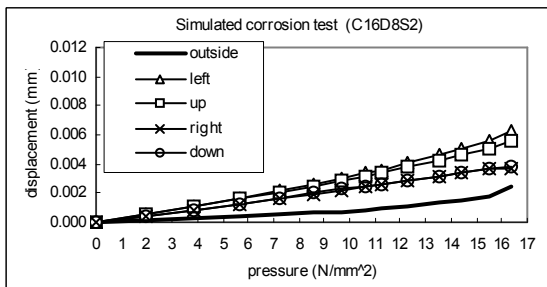Fig. 18. Net displacement -pressure curves of numerical result (C8D8S2).

Fig. 19. The reduction of the cover and elongation of the simulated bar.
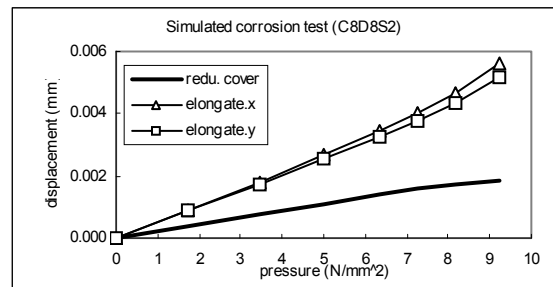

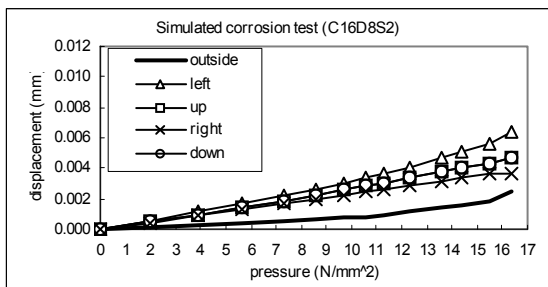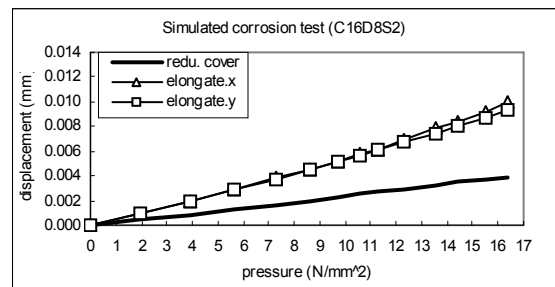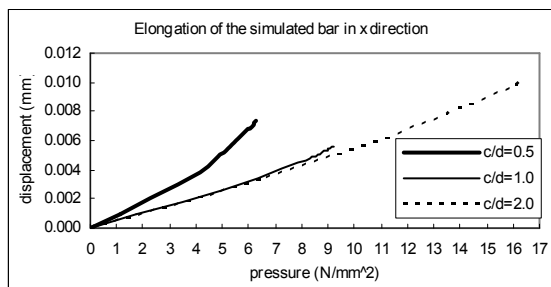Fig. 20. Displacement-pressure curves of numerical result (C16D8S2).

Fig. 21. Net displacement -pressure curves of numerical result (C16D8S2).

Fig. 22. The reduction of the cover and elongation of the simulated bar.

Fig. 23. The elongation of the simulated bar in x
direction.
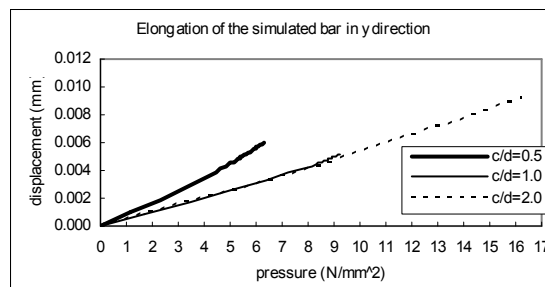
Fig. 24. The elongation of the simulated bar in y
direction.

5.3 Crack pattern and internal pressure

The crack pattern obtained from the numerical analysis for C4D8S2, i.e. c/d=0.5, are shown in Figures 25 ~ 27.

Figure 25 shows that the cracks appeared at the internal surface and the external surface of the concrete cover at the same load increment when the thickness of the concrete cover is smallest (4 mm). The magnitude of the internal pressure is 3.347 N/mm2 and the number of the load increment is = 3. As the internal pressure increase, the cracks from outside of the concrete cover progressed to join up with those from the inside of the concrete cover, which eventually penetrated the concrete cover as shown in Figure 26. The internal pressure increased to 4.147 N/mm2 . When the number of the load increment is 30, it can be observed that more cracks have appeared around the simulated bar and the concrete cover (Figure 27). After that, the arc-length method [5]

used in this investigation failed to trace further response due to convergence difficulties. An attempt was made in order to solve this convergence problem. However, as the source code of the arc-length method contained in LUSAS was not available, an examination on the source code was not possible. Nevertheless, the Author had taken various necessary steps in order to solve this problem that included reducing the load increment, increasing the number of iteration, adjusting the control parameters, etc. (see LUSAS User Manual). However, none of these steps were able to solve this problem.

The crack patterns obtained from the numerical analysis for C8D8S2, i.e. c/d=1.0, are shown in Figures 28 ~ 31.
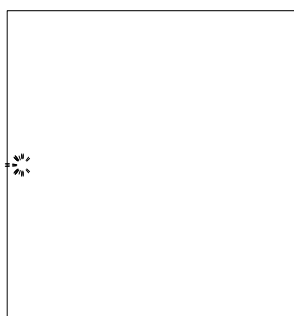

Fig. 25. Internal and external crack patterns of C4D8S2
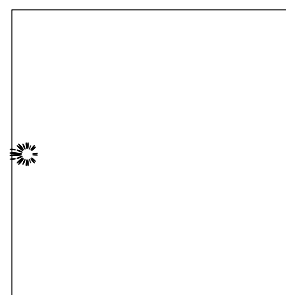(Increment = 3 ; Pressure = 3.35 N/mm2).

Fig. 26. Penetrating crack pattern of C4D8S2 (Increment
= 4 ; Pressure = 4.15 N/mm2).
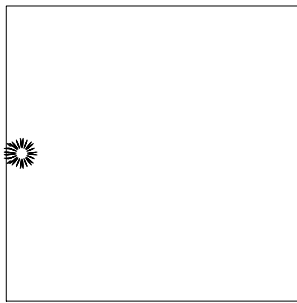
(Increment = 7 ; Pressure = 8.18).

Fig. 27. Final crack pattern of C4D8S2
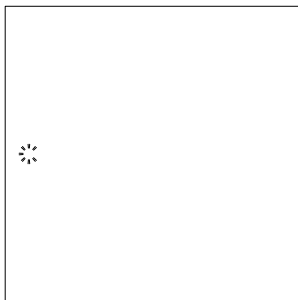(Increment = 30 ; Pressure = 6.36
N/mm2).

Fig. 28. Internal crack pattern of C8D8S2
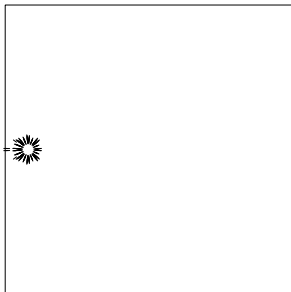(Increment = 2 ; Pressure = 3.44
N/mm2).

Fig. 29. External crack pattern of C8D8S2
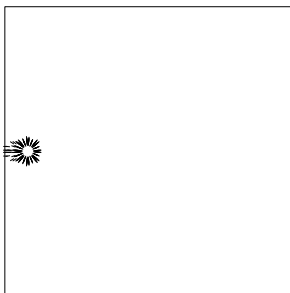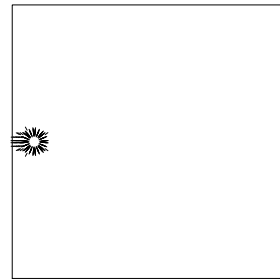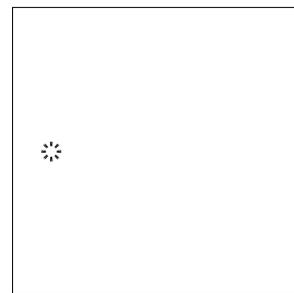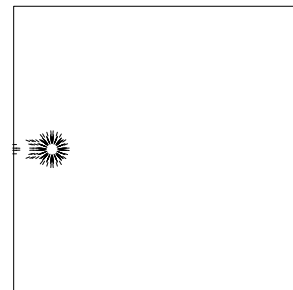(Increment = 6 ; Pressure = 7.9
N/mm2).

Fig. 30. Penetrating crack pattern of C8D8S2

Fig. 31. Final crack pattern of C8D8S2
(Increment = 38 ; Pressure = 9.22
N/mm2).

Fig. 32. Internal crack pattern of C16D8S2
(Increment = 2 ; Pressure = 3.89
N/mm2).

Fig. 33. External crack pattern of C16D8S2
(Increment = 18 ; Pressure = 15.48
N/mm2).

Figures 28 and 32 show that the cracks first appear at the internal surface of the concrete when the thickness of the concrete cover is 8 mm and 16 mm. The crack patterns follow similar progress as in test C4D8S2.
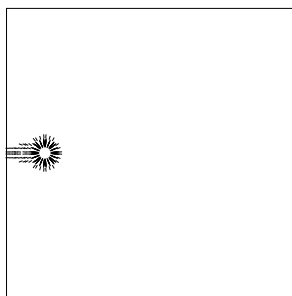
Fig. 34. Penetrating crack pattern of C16D8S2
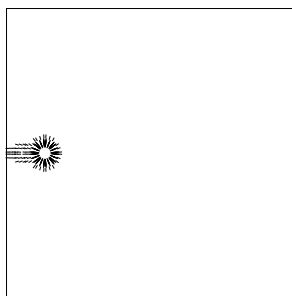(Increment = 21 ; Pressure = 15.93 N/mm2).

Fig. 35. Final crack pattern of C16D8S2
(Increment = 91 ; Pressure = 16.36
N/mm2) c/d=2.0, are shown in Figure
32 ~ 35.

Figures 31 and 35 show the final crack pattern at the load increment where the arc-length method failed to converge. Similar steps have been taken in order to solve this problem as given in C4D8S2, but these steps also failed.

For the three cover concrete ratios, i.e. c/d=0.5, 1.0 and 2.0, the arc-length method is not able to trace the ultimate pressure. However, when the internal pressure in which the crack pattern has penetrated the concrete cover is used to compare with the failure pressure obtained from the experiment, it can be seen that the internal pressure obtained from the numerical analysis shows good agreement with the experiment, as shown in Figure 36. It is possible that when the crack pattern penetrates the concrete cover, the specimen is not able to resist further pressure. A further increment of internal pressure would split the concrete cover and lead to a release of all of the internal pressure. This is supported by the experimental result (for c/d=2.0) where a splitting crack pattern around the concrete cover (Figure 3) is seen.

Figure 36 also shows that, in both the experimental and the numerical results, the failure pressure increases with c/d ratio.

Figure 37 shows the comparison of the results of the internal pressures which include the internal pressures at which the cracks were predicted to appear at the internal surface, external surface and penetrated the concrete cover with concrete cover = 4, 8 and 16 mm. It can be seen that both the internal pressures at which the cracks appeared at the external surface and at which they penetrated the concrete cover show that the internal pressure increases with c/d ratio. However, the internal pressure at which the cracks appeared at the internal surface is independent of the c/d ratio.
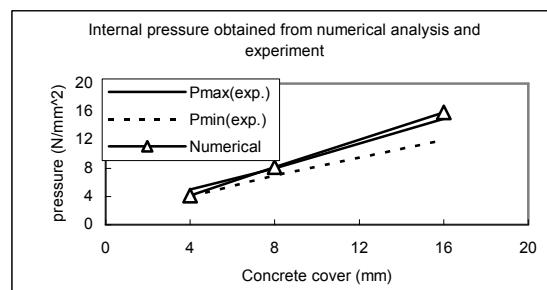

Fig. 36. The failure pressure of the numerical
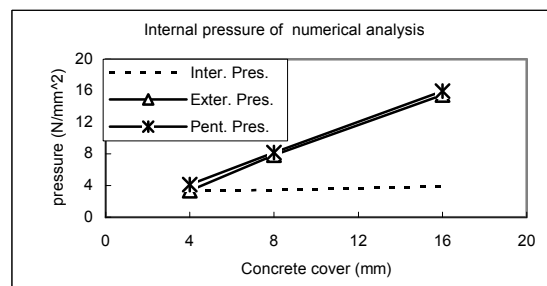and experimental result with concrete cover
= 4, 8 and 16 mm.

Fig. 37 The internal pressure of the numerical result
with concrete cover = 4, 8 and 16 mm.

Fig. 38. Load increment = 2

Stress distributions of C4D8M2
Principal stress = 1.50 - 2.16 N/mm2.

5.4 Stress distribution

The stress distribution of C4D8S2 obtained from the numerical analysis are plotted in Figures 38 ~ 41. Only the area that contains the higher principal stress is plotted. Figures 38 ~ 41 show that the area with higher principal stress is almost the same with the numerical crack patterns (Figures 25 to 27). The reason is that the maximum principal stress criterion is used in this crack model.

The stress distribution of C8D8S2 and C16D8S2 are not shown as again, the area with higher principal stress is almost the same with the numerical crack patterns.
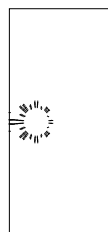

Fig. 39. Load increment = 3
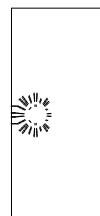
Stress distributions of C4D8M2.

Fig. 40. Load increment = 4

Stress distributions of C4D8M2.

Fig. 41. Load increment = 30

Stress distributions of C4D8M2
Principal stress = 1.50 - 2.16 N/mm2.

5.5 The influence of the boundary condition

In order to investigate how the boundary condition could affect the behaviour of the corrosion specimen, another set of numerical analysis was carried out which altered the roller support of the specimen to a hinge support (Figure 10).

The crack patterns, stress distributions, internal pressures, reduction of the concrete cover and the expansion of the simulated bar for x and y directions obtained from this case (hinge support) were used to compare with the previous case (roller support). The numerical results of the above issues obtained from these two boundary conditions are almost identical. Figure 42 showed the deformed meshes of the two boundary conditions. It confirmed that the expansion with the simulated bar of the two boundary conditions are almost identical.
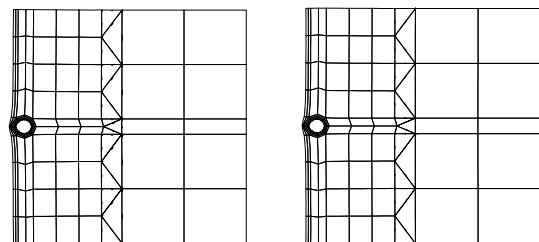
Boundary: Free(Roller)   Boundary: Fixed(Hinge)

Fig. 42. Deformed mesh of C4D8M2.

Nevertheless, there are significant differences in the displacement-pressure curves obtained from the two boundary conditions. Figures 43 to 45 show the displacement-pressure

curves obtained by plotting the displacement of the outside point (see Figure 10) vs. the internal pressure. It can be seen that, for the three c/d ratios, the case I (roller support) has a higher displacement than the case II (hinge support). Figures 46 to 48 show the displacement-pressure curves obtained by plotting the displacement of the center point (see Figure 10) in the x direction vs. the internal pressure. Again, it can be seen that, for the three c/d ratios, the case I (roller support) has a higher displacement than the case II (hinge support). Figures 49 to 51 show the displacement-pressure curves obtained by plotting the displacement of the center point (see Figure 10) in the y direction vs. the internal pressure. Only the results for the case I (roller support) are plotted because the displacements in the y direction for case II (hinge support) are almost zero.
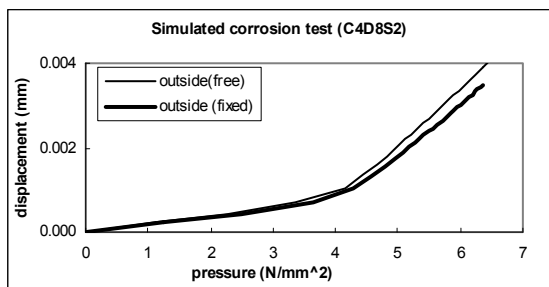

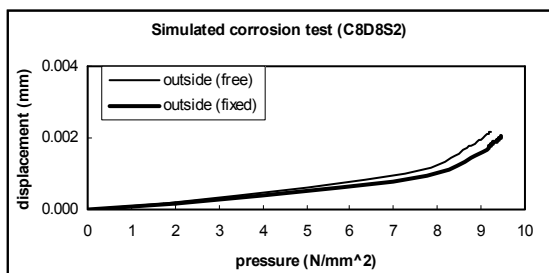Fig. 43. Displacement-pressure curves of different boundary conditions (C4D8S2).

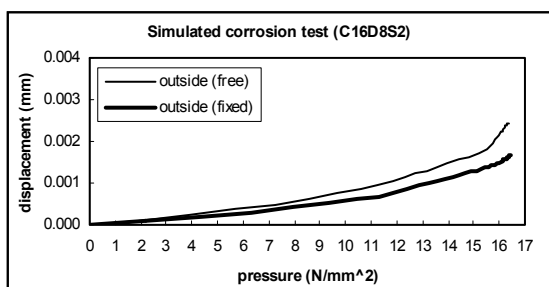Fig. 44. Displacement-pressure curves of different boundary conditions (C8D8S2).

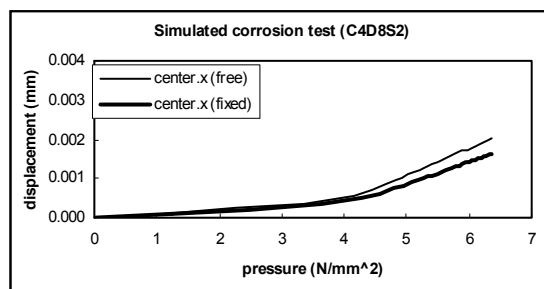Fig. 45. Displacement-pressure curves of different boundary conditions (C16D8S2)

Fig. 46. Displacement-pressure curves of different boundary conditions (C4D8S2).
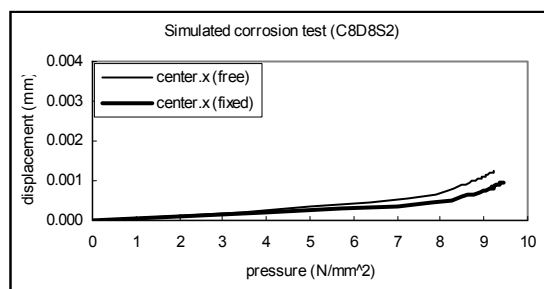

Fig. 47. Displacement-pressure curves of different boundary conditions (C8D8S2).
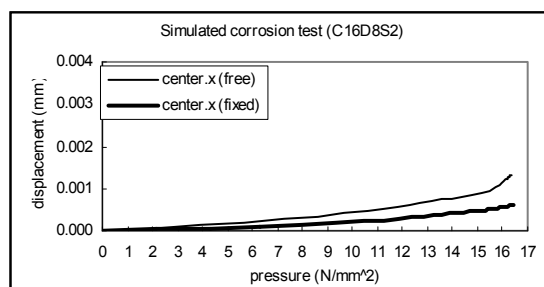

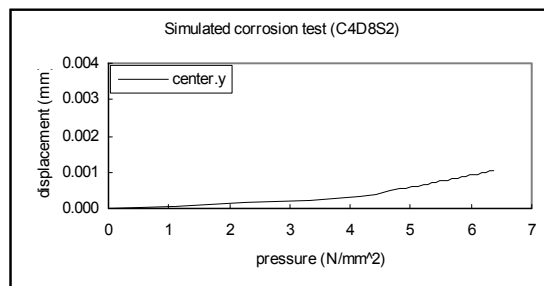Fig. 48. Displacement-pressure curves of different boundary conditions (C16D8S2).

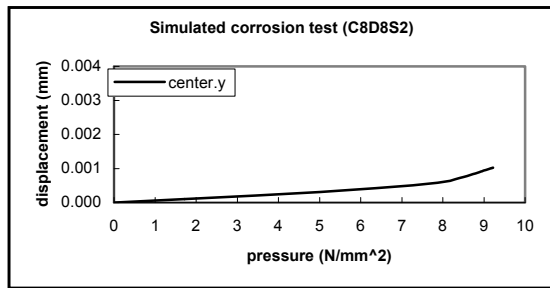Fig. 49. Displacement-pressure curve for roller support (C4D8S2).

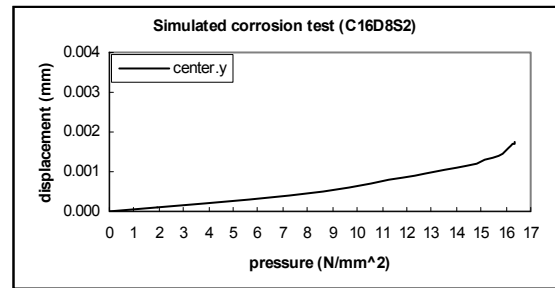Fig. 50. Displacement-pressure curve for roller support (C8D8S2).

Fig. 51. Displacement-pressure curve for roller support (C16D8S2).

VI. CONCLUSION

1. The failure pressures obtained from the numerical analysis agree well with the experiment. In addition, both the experiment and the numerical simulation showed that the failure pressure increases with increasing c/d ratio.
2. The results of the numerical analysis show that the assumption of uniform bar expansion is reasonable.In addition, the crack patterns, stress distributions, internal pressures, reduction of the concrete cover and the expansion of the simulated bar for x and y directions are almost identical with the two boundary conditions.
3. The direction of the movement of the simulated bar is not the same with the two boundary conditions. The simulated bar in case I (roller support) appears to move larger distance than that of the case II (hinge support). Nevertheless, the numerical results show that the failure mechanics of these two boundary conditions are identical.

ACKNOWLEDGEMENTS

REFERENCE

[1] FEA Ltd. Lusas User Manual (version 12.3), London, England, 2007
[2] Williamson SJ and Clark LA, Influence of Concrete Quality on the Effects of Reinforcement Corrosion. Proceedings of the Seventh International Conference on Structural Faults and Repairs, Vol.1, pp. 441-446, 1997
[3] Bazant, Z. P. and Cedolin, L., "Fracture mechanics of reinforced concrete." Journal of the Engineering Mechanics Division, ASCE, 106, pp. 1287-1306, 1980.
[4] Bazant, Z. P., and Oh, B. H., "Crack band theory for fracture of concrete." Materials and Structures RILEM, Vol.16, pp. 155-177, 1983.
[5] Cervera, M., Hinton, E., and Hassan,O., "Nonlinear analysis of reinforced concrete plate and shell structures using 20-noded isoparametric brick elements." Computers and Structures, Vol. 25, No. 6, pp. 845-869, 1987.
[6] Jefferson, A. D., and Wright, H. D., "Stepped softening function for concrete fracture in finite element analysis." Computers and Structures Vol. 41, No. 2, pp.331-344, 1991.
[7] Lotfi, H. R., and Shing, P. B., "An Appraisal of Smeared Crack Models for Masonry Shear Wall Analysis." Computers and Structures, Vol. 41, pp. 413-425, 1991.
[8] Tuutti K, Corrosion of steel in concrete. Swedish Cement and Concrete Research Institute, 1982.
[9] Nilsson, L., and Oldenburg, M., "Non-linear Wave propagation in plastic fracture materials-a constitutive modeling and finite element analysis." IUTAM symp on Non-linear Deformation Waves, Tallin, 1982.
[10] Owen, D. R. J., Figueiras, J. A., and Damjanic, F., "Finite element analysis of reinforced and prestressed concrete structures including thermal loading." Computer Methods in Applied Mechanics and Engineering Vol. 41, pp. 323-366, 1983.
[11] Kupfer, H. B., Hilsdorf, H. K., and Rusch, H., "Behaviour of concrete under biaxial stresses. Proceeding." American

Concrete Institute Vol. 66, No. 8, Aug., 656-666, 1969.

[12]   Sinha, B. P., Gerstle, K. H., and Tulin, L. G., "Stress-strain relations for concrete under cyclic loading." Journal of the American Concrete Institute February, Vol. 61, No. 2, pp. 195-211, 1964